NASA-CR-194776

FINAL
IN-91-CR
OCIT
198584
32P

FINAL REPORT

NASA Grant NAG5-537

Voyager Planetary Radio Astronomy Studies

Covering the period

May 1, 1985 to June 30, 1993

Submitted by:

David H. Staelin
and
Stephen S. Eikenberry

Research Laboratory of Electronics
Massachusetts Institute of Technology
Cambridge, Massachusetts 02139

December 23, 1993

(NASA-CR-194776) VOYAGER PLANETARY
RADIO ASTRONOMY STUDIES Final
Report, 1 May 1985 - 30 Jun. 1993
(MIT) 32 p

N94-24328

Unclas

G3/91 0198584

Voyager Planetary Radio Astronomy Studies

Table of Contents

Voyager Planetary Radio Astronomy Studies

I. Introduction

This grant has supported analysis of nonthermal radio emission data obtained by the Planetary Radio Astronomy (PRA) spectrometers on the Voyager 1 and 2 spacecraft. This PRA data has provided unique insights into the radio emission characteristics of the outer planets because of PRA's unique spectral response below the terrestrial ionospheric plasma frequency and its unprecedented proximity to the source. Of those results which have been documented or published, this final report surveys only the highlights and cites references for more complete discussions. Unpublished results for Uranus, Neptune, and theoretical Ionian current distributions are presented here at greater length.

The most important conclusion to be drawn from these observations is that banded spectral emission is common to the radio emission below 1-2 MHz observed from all four Jovian planets. In every case multiple spectral features evolve on time scales of seconds to minutes. To the extent these features drift in frequency, they appear never to cross one another. The Neptunian spectral features appear to drift little or not at all, their evolution consisting principally of waxing and waning. Since other evidence strongly suggests that most or all of this radio emission is occurring near the local magnetospheric electron cyclotron frequency, this implies that this emission preferentially occurs at certain continually changing planetary radii. It remains unknown why certain radii might be favored, unless radial electric field components or other means serve to differentiate radially the magnetospheric plasma density, particle energy vectors, or particle coherence. Calculations of the spatial distribution and intensity of the Io-generated magnetospheric currents are also presented; these currents may be limited principally by wave impedance and local field strengths.

II. Jovian and Saturnian Nonthermal Radio Emission - Observational Studies

A. Jovian Arcs

Our first study of Jovian nonthermal radio emission focused on the prominent "arcs" which appear when the PRA radio intensity at 1-40 MHz is displayed in time-frequency coordinates; this work was a continuation of earlier studies. These arcs can be divided into two categories, called "vertex-early" and "vertex-late," where the vertex-early arcs are initially observable at an intermediate frequency (the "vertex frequency") which then bifurcates and simultaneously drifts both upward and downward in frequency until the emission ends. Vertex-late arcs appear reversed in time; two frequencies are observed initially and these merge at the vertex frequency and cease. Both types form a continuous arc of emission which resembles a crescent moon in the frequency-time domain.

The first publication of this work was "Jovian Decametric Arcs and Alfvén Currents" by Staelin et al. (1988). The most important observation of this study was perhaps the systematic variation of vertex frequency with Jovian longitude. In particular, the right-circularly-polarized arcs typically exhibit vertex frequencies which declined from ~25 MHz to 5 MHz as the Jovian longitude (central meridian longitude of the spacecraft) increased from 90° to 180°; the vertex-late arcs exhibited a similar decline in vertex frequency, but offset approximately 130° more in longitude. These offsets of ~120° - 140° are consistent with a hollow cone of radio emission aligned with the local magnetospheric field and flared outward at a half angle of ~70° - 90°. The arc shape could plausibly be the result of systematically larger flare angles near the vertex frequency. Possible mechanisms for this were discussed by Goldstein et al. (1979), Staelin (1981), Goldstein and Thieman (1981), Hashimoto and Goldstein (1983), and others, but they remain speculative. Histograms of the vertex frequency relative to the presumed longitude L of the cone axis (where $L \cong 256° - 4.56f_V$; f_V is the vertex frequency (MHz)) suggest that typical cone half angles projected on the Jovian equator (i.e., perceived by Voyager) are ~50° - 90° and that they seldom exceed 90°. In fact, the relation between vertex frequency and longitude may be relatively more stable than the projected cone half angle, which appears to vary ±20°.

Gurnett and Goertz (1981) have suggested that these multiple arcs may be produced by multiply-reflected Alfvén waves travelling along magnetospheric field lines between hemispheres where they are reflected by the ionosphere. Such magnetospheric Alfvén waves are expected from Io's motion relative to the Jovian magnetic field. The observed occurrence of arcs, which is almost uniform over all longitudes, suggests a very long lifetime for such reflected Alfvén waves, generally more than one Jovian rotation period, while statistical distributions of these arcs suggest their vertices are Poisson distributed in time with an average of 3.2 events per minute. Such a random distribution could occur if the presumed cone half angle varied randomly over angles larger than the angle in longitude between successive reflected Alfvén waves, or if such Alfvén waves continued to generate arcs over several rotations of the planet.

Somewhat similar arcs composed of S-burst events have been observed at Nancay (Leblanc, 1981; Leblanc and Genova, 1981). These arcs appear to cluster strongly near Jovian central meridian longitudes of 145°, within a band less than 90° wide. These same S-burst arcs also occurred only when the phase of Io was 80° - 105°, except for a few near 233°. Additional discussion of these results was reported by Garnavich (1983) and Staelin et al. (1988).

B. Striated Spectral Activity from Jupiter and Saturn

Another new phenomenon studied was "Striated Spectral Activity in Jovian and Saturnian Radio Emissions" reported by Arias (1986) and Thieman et al. (1988). The high-time-resolution frequency-time spectrograms of radio emission observed near the Voyager 1 and 2 encounters with Jupiter reveal occasional striation patterns within the normally diffuse hectometric radiation. Distinctive banded structures of enhanced intensity meander in frequency over time scales of minutes to tens of minutes. This banded form of striated spectral activity (SSA) occurs roughly 5 percent of the time during the three weeks before and after Jupiter encounters. Banded SSA is often preceded or followed by a chaotic form of SSA where the banding of the emission becomes discontinuous or unrecognizable although the quasiperiodic intensity modulation with frequency is still evident for each single 6-s frequency sweep of the PRA instrument. Although SSA normally occurs at frequencies of ~0.2-1.0 MHz, similar but longer-lasting patterns have been found occasionally in decametric emission above 10 MHz. Analogous modulation was also observed near Saturn, suggesting that SSA may be intrinsic to the radio emission at both planets.

Plots of single 6-s frequency sweeps often exhibit a slow rise in intensity, followed by a sharp decline at the edge of each band as frequency decreases. This sawtooth form of the spectrum is evident in both planets, but is difficult to explain theoretically.

Although Jovian hectometric banded SSA is observed to occur only 4.5 percent and 8.1 percent of the time pre-encounter for Voyager 1 and 2, respectively, and 1.6 percent and 3.0 percent post-encounter, there was no clear relation between these occurrences and the central meridian longitude of Jupiter as seen by Voyager, or with respect to Io phase alone. This work is described more fully by Thieman et al. (1988). Evans et al. (1987) presented Uranian kilometer radiometric observations reminiscent of the SSA observed at Jupiter and Saturn.

III. Uranian Nonthermal Radio Emission

A. Introduction

The Uranian PRA data were more limited but also reveal a variety of radio emission morphologies. Most important was the overall intensity modulation with a period near 17 hours, identified as the rotation period of the Uranian magnetic field. These results, supported partly by this effort, were described in part by Warwick et al. (1986).

The data for Uranus and Neptune were recorded by PRA in its standard 6-second 198-channel format in which the frequency steps every 6 seconds from 1.2 kHz to 1.3 MHz, with 19.2-kHz channel separation and 1-kHz bandwidths, alternating between left- and right-hand polarization for successive frequencies. On alternate sweeps the polarization for each channel is reversed, producing a checkerboard of polarizations in the time-frequency plane. We did not analyze Uranian or Neptunian observations above 1.3 MHz.

Narrowband strongly polarized radio bursts from Neptune were observable by Voyager 2 for more than a 50-day period, ranging from 100 to 1300 kHz. Smoother emission from 20-865 kHz was observable for about 10 days near closest approach, implying a rotation period of ~16 hours. These additional results were described by Warwick et al. (1989).

Most prior analyses of these data dealt with the physical location and beaming properties of the emission sources and with their gross spectral properties, such as central frequency and bandwidth. We concentrated on the detailed morphology of the Uranian spectra using the full 19.2-kHz and six-second resolution of the PRA instrument, and noted similarities with the striated spectral activity often observed near Jupiter and Saturn (Thieman et al., 1988). The data analyzed comes from two days before closest approach to seven days after (January 22 to January 31, 1986.) The strongest spectra were observed during the 3-day period immediately following the encounter, and most of the analyzed features occurred during this period. Virtually all of the Uranian emissions were below 1 MHz in frequency.

The Uranian spectra consist mainly of bands with widths varying from a few to several hundred kilohertz. These phenomena exist on time scales ranging from a few minutes up to nearly an hour, and often change their characteristics over this span. The major categories of emission spectra are characterized here as constant uniform striations, drifting uniform striations, chaotic striations, split high- and low-frequency groups, and high-frequency cutoffs. Several of these categories, particularly the uniform striations, resemble the striated spectral activity (SSA) observed at Jupiter and Saturn by Voyagers 1 and 2.

Section B describes the format and reduction of the Uranus PRA data. Section C discusses the basic features and variations of each of the five categories of the emissions, while Section D examines the statistics of their occurrences and transitions between them.

B. Data Reduction Techniques

The data were obtained by Voyager 2 during an interval from January 22 (two days before closest approach) to January 31 (seven days after). Closest approach to Uranus occurred on January 24, 1986 at 1759 UCT (coordinated universal time) (Stone and Miner, 1986). The data were recorded in the standard six-second, 198-channel format used by the PRA instrument. In this mode the PRA receiver steps every six seconds from 1.2 kHz to 1.3 MHz, with 19.2-kHz channel separations and 1-kHz channel bandwidths, alternating between right- and left-hand polarization for successive frequencies. On alternate sweeps the polarization for each channel is reversed, producing a checkerboard of polarizations in time-frequency coordinates. Observations above 1.3 MHz were not analyzed in this study. A more complete description of the PRA instrument has been presented by Lang and Peltzer (1977).

We processed the data in 51-minute blocks. Reduction of the data involved three steps. The first step removed the polarization checkering and scattered noise. Each pixel in the time-frequency domain was encoded with values for power and polarization. The value of each pixel was averaged with its nearest neighbors in time, both before and after, using a 1-2-1 weighting scheme. Thus the new value of each pixel equally represented right-polarized and left-polarized power, yielding a spectral image normalized with respect to polarization. Then the 5 highest and 5 lowest-valued pixels in intensity were deleted, two percent of the data, in an attempt to remove noise spikes.

The images produced by this process exhibited Uranian emission, but were still marred by interference that made them unusable for spectral analysis. This interference was comprised of two main categories. One consisted of high intensity pulses about 2 minutes in duration and occupying the entire bandwidth of the PRA instrument. The second possessed narrower bandwidths (usually 20-40 kHz, though occasionally up to 600-800 kHz) that were stable in frequency on a time scale of hours.

The second step in reducing the Voyager data involved removal of the two-minute bursts of broadband spacecraft interference; they were relatively periodic in their appearances. They were manually deleted and replaced with values of zero intensity.

The third step in data reduction was the removal of the narrowband constant-frequency interference spikes together with the drifting noise baseline. In a region free of Uranian emissions, discernible by their cloud-like features and drifts in frequency, an average spectrum was taken over a two-minute interval. This spectrum, approximating the noise floor, was then subtracted from each of the six-second spectra in the 51-minute image. The resulting images were nearly noise-free. Although some ghosts of the interference spikes remained, these were usually very faint and distinguishable from the Uranian emissions by their lack of variation in intensity and frequency. Some negative values were inadvertently set to zero, which has made unambiguous interpretation of the Uranus and Neptune observations difficult.

C. Spectral Phenomenology

The Uranian radio emissions can be placed in five largely distinct classes according to their spectral properties. The first class, uniform constant striations, are recognizable by their multiple high-intensity bands that are nearly constant in frequency over periods of a minute or more (Figure 1).

The second class, uniform drifting striations, are similar to the first in most respects, except for their increased tendency to wander in frequency over periods of a few seconds (Figure 2).

One step beyond this lies the third class of spectral activity, chaotic striations (Figure 3), for which wanderings become so rapid and random that

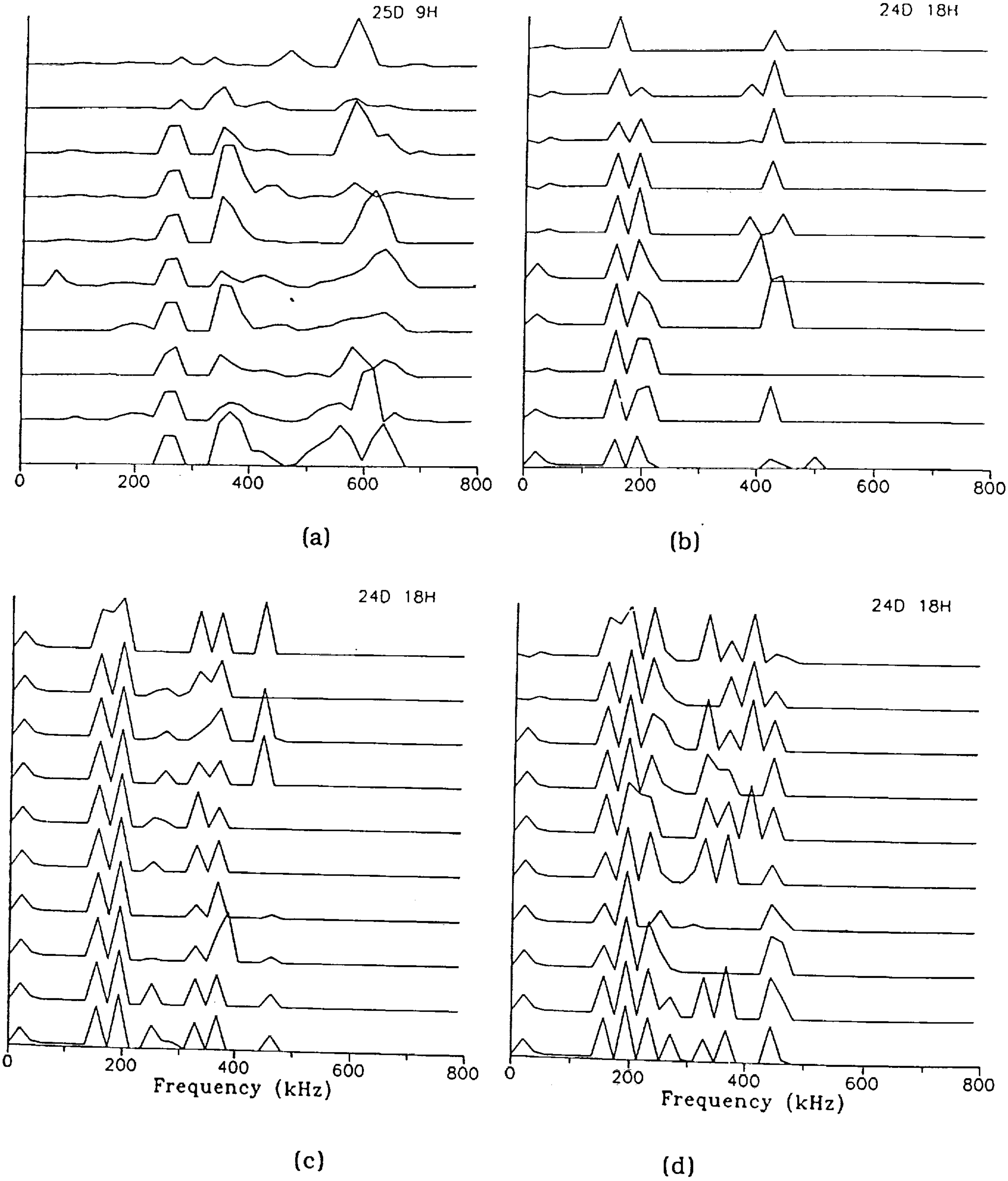

Figure 1. Uniform constant striations in Uranian emissions.

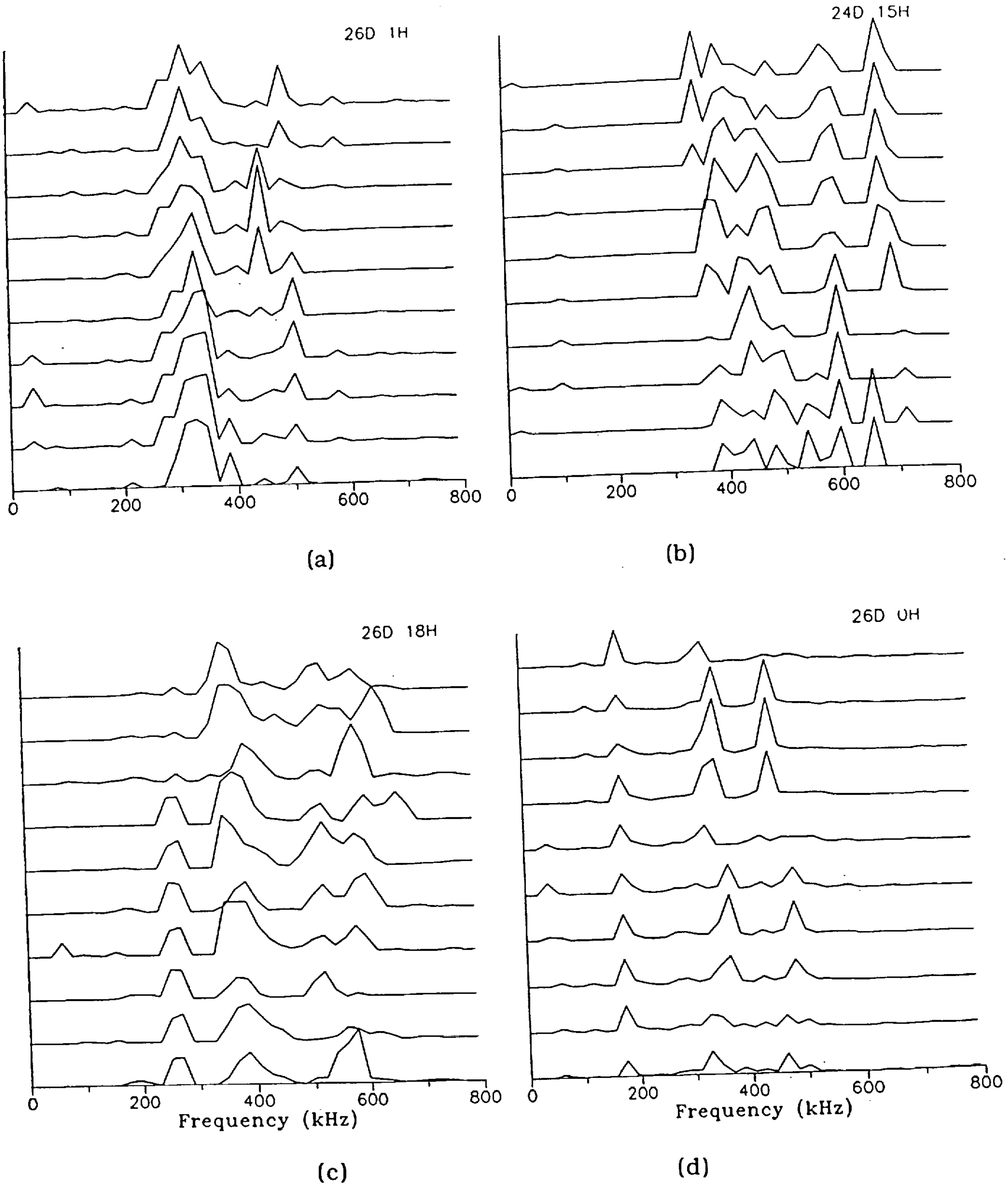

Figure 2. Uniform drifting striations in Uranian emissions.

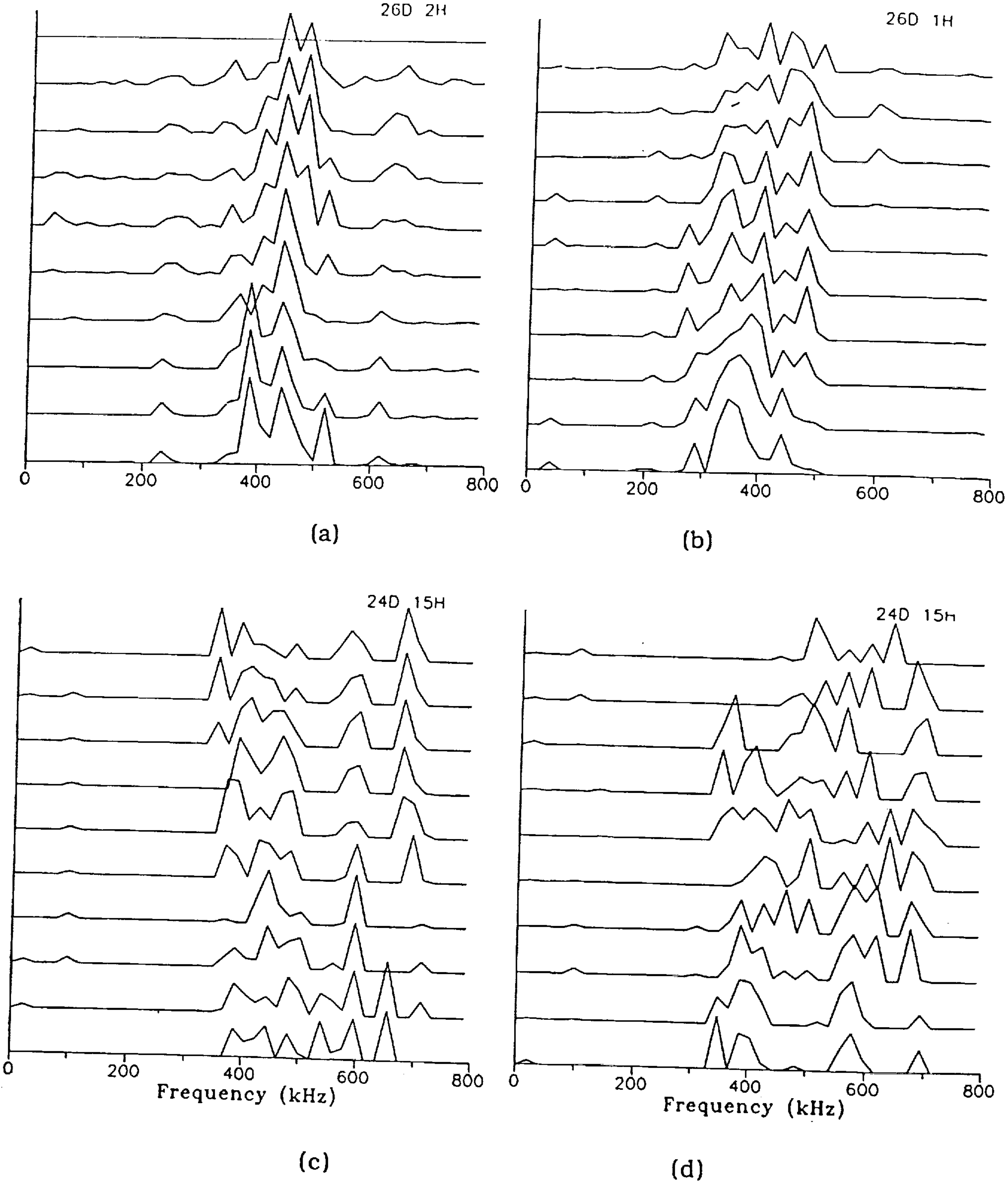

(a) (b)

(c) (d)

Figure 3. Chaotic striations.

the banding pattern seen in one six-second spectrum is unrecognizable in the next.

A fourth class is formed by those spectra whose chief characteristic is that they exhibit a sharp drop in intensity at their high frequency end (Figure 4).

Occasionally individual striations are separated by large bands of very low intensity. These two striated bands exhibit characteristics similar to those in the first four classes. Such high-low splitting comprises the fifth spectral class (Figure 5). Each of these classes warrants individual investigation.

The most prominent characteristics of the first class of emissions, uniform constant striations, is the persistence of several bands of high intensity at the same frequency over periods of time on the order of minutes. In Figure 1a, the bands at 250 and 350 kHz remain relatively stable, while a feature at 600 kHz drifts approximately 120 kHz in 18 seconds and changes in intensity. Twin peaks between 100 and 200 kHz remain steady in both Figures 1b and c, while the higher frequency component of b (f = 420 kHz) drifts 20 kHz (one channel) over 30 s, and the upper components in c (f = 300 - 400 kHz) remain rather still. In Figure 1d, the highest (450 kHz) and two lowest (150 and 200 kHz) frequency striations do not change, whereas the intervening striations shift in both form and frequency, even temporarily disappearing part-way through the figure.

The second class of spectral phenomena, that of uniform drifting striations, is closely related to the first class. They too consist of high-intensity bands with a striated pattern recognizable from spectral frame to spectral frame. However, these bands appear to shift noticeably in their patterns, often developing into new patterns over a period of several minutes. Figure 2a illustrates the basic features of this class. The component at 300-350 kHz drifts only 20 kHz (the resolution limit of the receiver), most of the changes being manifested in the form. Meanwhile, the band that starts near 500 kHz drifts down in frequency until its lower end (which has decreased a factor of 7 in intensity) is below 450 kHz, a change of 50 kHz. In Figure 2b the three distinct bands at 400-450, 600, and 700 kHz, respectively, contract towards their center for the first 36 seconds (the total bandwidth decreases from 390 kHz to 360 kHz). Panel c of the figures similarly suggests combinations of drifting on the order of 50 kHz. The fourth group, panel d, on the other hand, more closely resembles the first class of spectra in that the two components near 350 and 450 kHz drift synchronously. As the spectral striations move farther and more rapidly in frequency, they begin to form a third class of spectra.

Chaotic striations are the third class in this progression from stable spectral bands to drifting striations, and finally to disorder. In panel a of Figure 3 a pattern of fairly uniform bands persists at 450 to 500 kHz for about 20 seconds. However, they then begin changing such that 40 seconds later a new pattern of three distinct high-intensity bands has come into existence. In panel b,

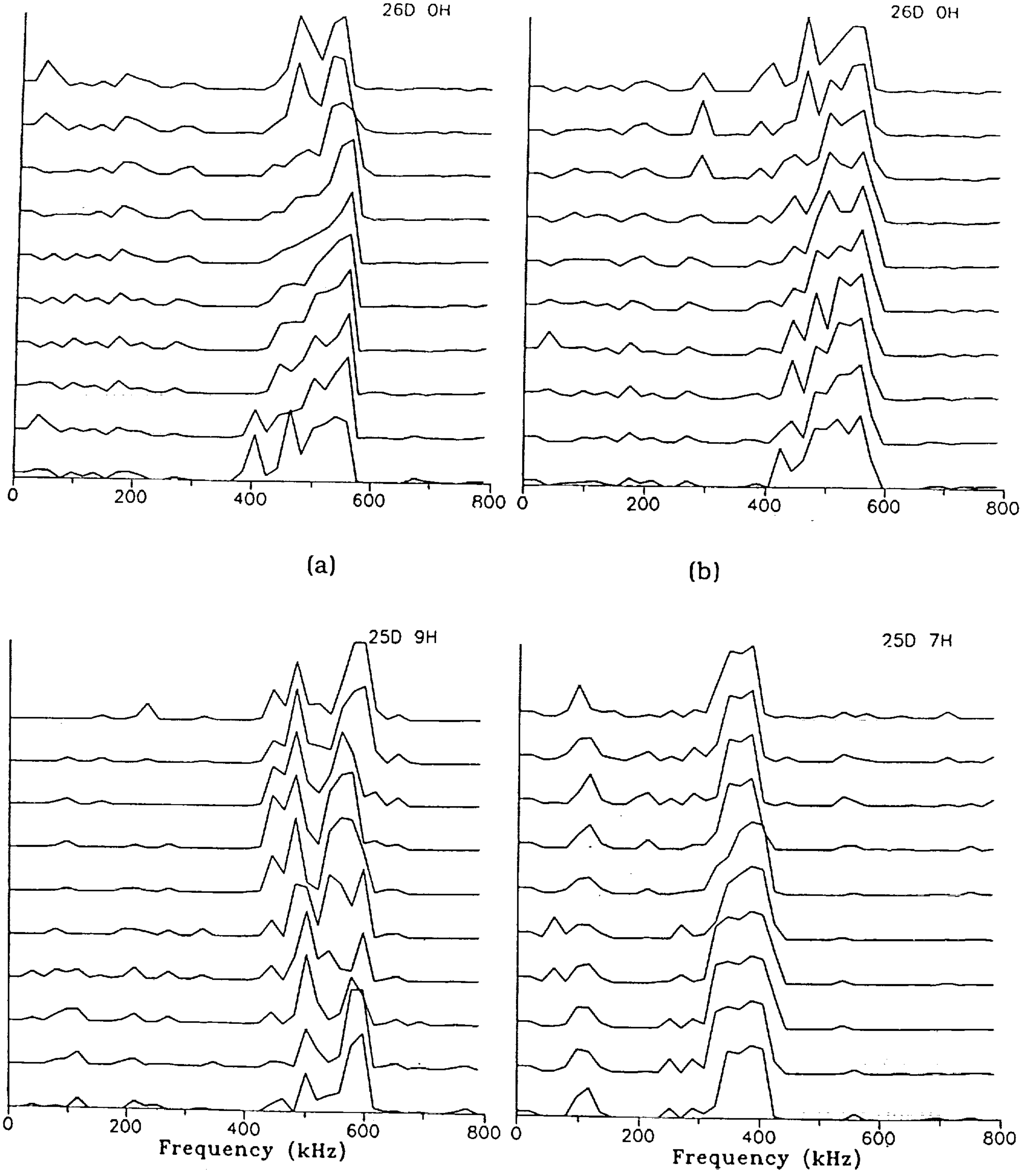

(a) (b) (c) (d)

Figure 4. High-frequency cutoff.

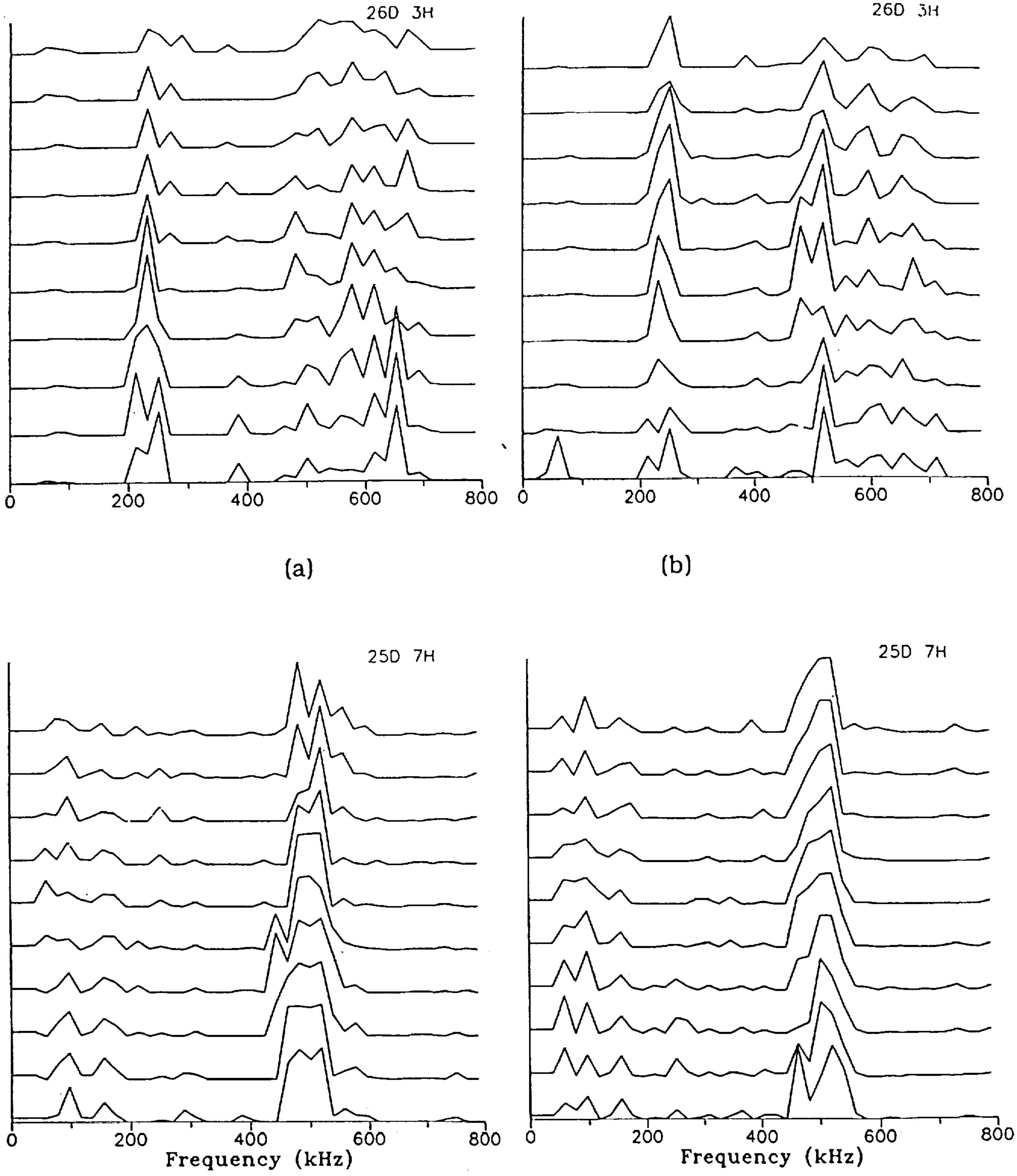

(a) (b)

(c) (d)

Figure 5. High-low split Uranian emission.

a group of four to five striations centered at 400 kHz mutates into a group of two narrow and one broad band. Panel c (the same as Figure 2b) begins with class-two drifting and a uniform pattern of striations. Yet, in a matter of 30 seconds, it transforms into a spectrum unrelated to its parent. The fourth panel, Figure 3d, is much more chaotic.

The most striking feature of the fourth class of Uranian spectrum is the sharp drop in power at high frequencies within 50 kHz, and most cutoffs occur in a much narrower bandwidth. The spectra in Figure 4a typify this class, with low intensities from 1 to 400 kHz, and then a gradually sloping increase to a high intensity near 550 kHz, followed by a sudden drop to zero intensity within the bandwidth of only one channel, 19.2 kHz. Panels b and c closely resemble panel a, and decay over two and one channels respectively. The low frequency side of these examples exhibit chaotic and uniform drifting striations, respectively. Figure 4d displays a high frequency cutoff near 400 kHz and a drifting feature near 100 kHz.

The fifth and final class of Uranian radio spectra exhibits separation of 200-300 kHz between two groups of features. Often one group will have a single band while the other group will display multiple striations, though there are cases in which neither or both groups have more than one band. In Figure 5, panels a and b exhibit single striations in the low frequency region, 200-275 kHz, while displaying multiple striations in the high frequency region, 500-700 kHz. In panels c and d, the reverse is true, with multiple bands in the 50-200 kHz range, and single striations in the 400-600 kHz range.

D. Patterns in Spectra

Patterns in the occurrence of the various spectral types were sought. First the longitudes of Voyager 2 at the time it detected each class were studied. The histogram in Figure 6 depicts the occurrences of emission versus longitude, in the ULS coordinate system described by Kaiser, et al. (Kaiser et al., 1987). We now define Type 1 emission to include both the constant and drifting uniform striations that make up spectral classes 1 and 2. These classes were merged because they behave similarly and sometimes are difficult to distinguish. Types 2, 3, and 4 correspond to classes 3, 4, and 5, respectively. Type 5 is defined as the quiet state. The sample of emissions obtained by Voyager 2 at Uranus includes a total of 62 distinct events, comprising over 85 percent of the available data. Although this set is too small to permit detailed statistical analysis, the emissions are obviously grouped from about 0 to 120 degrees longitude. These longitudes are roughly centered on 48 degrees, the longitude of the south pole of Uranus' tilted magnetic field (Ness et al., 1986). Interestingly, directly over the pole the Type 4 (high-low splitting) phenomena are less likely to appear, while Type 1 events become most likely. Lack of data prevents a conclusive interpretation.

Another interesting pattern lies in the statistics for transitions between various classes of spectral emission. Table 1 represents a matrix characterizing

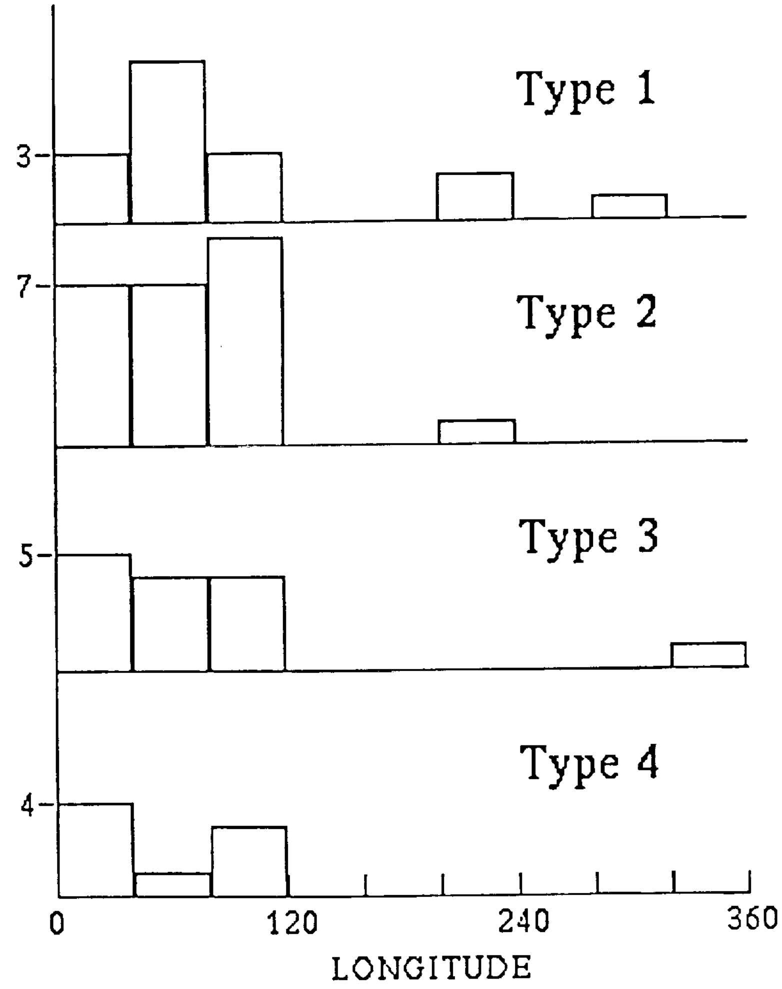

Figure 6. Distribution in longitude of various emission types.

the statistical probabilities of a transition from one state to another. The probabilities are normalized to represent percentages of transitions to each destination state; they are "destination normalized" so that all the transitions to a given state sum to 100 percent. Table 2 is a similar matrix with the probabilities "source normalized". In these tables, a transition between states occurs if the emission is in a given state for any length of time.

By requiring the emission to adhere to a given spectral form for a certain amount of time before it can be considered to occupy that state, we can calculate a transition matrix such as the one in Table 3. Here the time of occupation is one minute. If the emission remains in that state for two minutes, then it is considered to have made a transition into itself, which is the significance of the diagonal values of the matrix. Figures 7 and 8 are flow diagrams coded according to the probabilities in Tables 1 and 2, respectively. The most immediately noticeable aspect of both such charts is that all states often lead to one another, with two exceptions. For the limited data set here, Type-4 emissions never evolve into Type 2, and Type 3 never evolves into Type 1.

Table 1. Destination-Normalized State Transition Probabilities (Percent)

		Final State				
		1	2	3	4	5
Initial	1	-	41	26	18	14
State	2	44	-	24	24	20
	3	0	19	-	21	36
	4	18	0	30	-	31
	5	38	40	20	38	-

Table 2. Source-Normalized State Transition Probabilities (Percent)

		Final State				
		1	2	3	4	5
Initial	1	-	44	22	6	28
State	2	32	-	20	8	40
	3	0	20	-	7	73
	4	13	0	25	-	63
	5	27	43	17	13	-

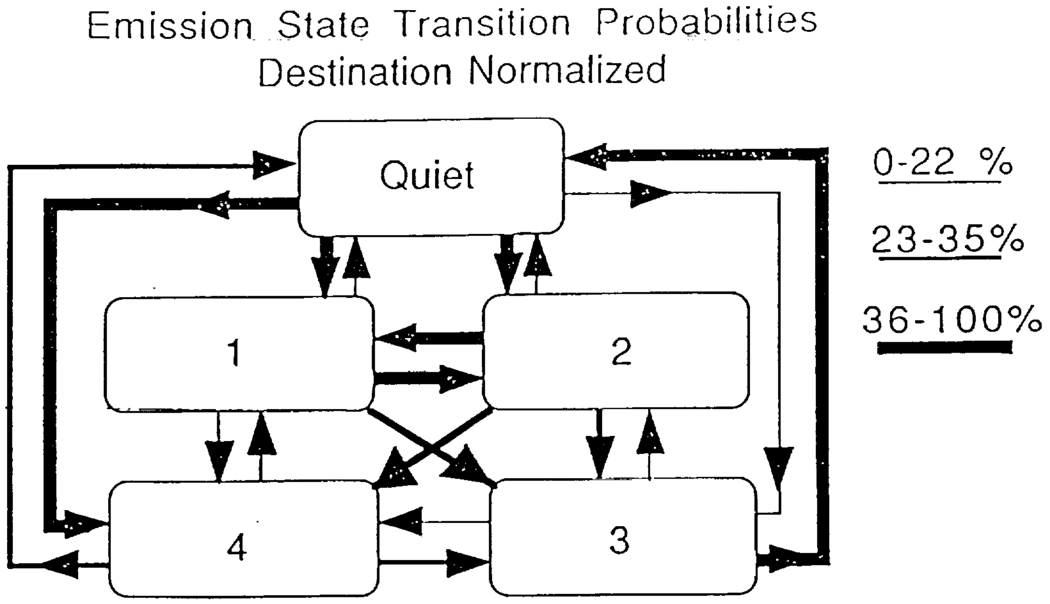

Figure 7. Emission state transition probabilities, destination normalized.

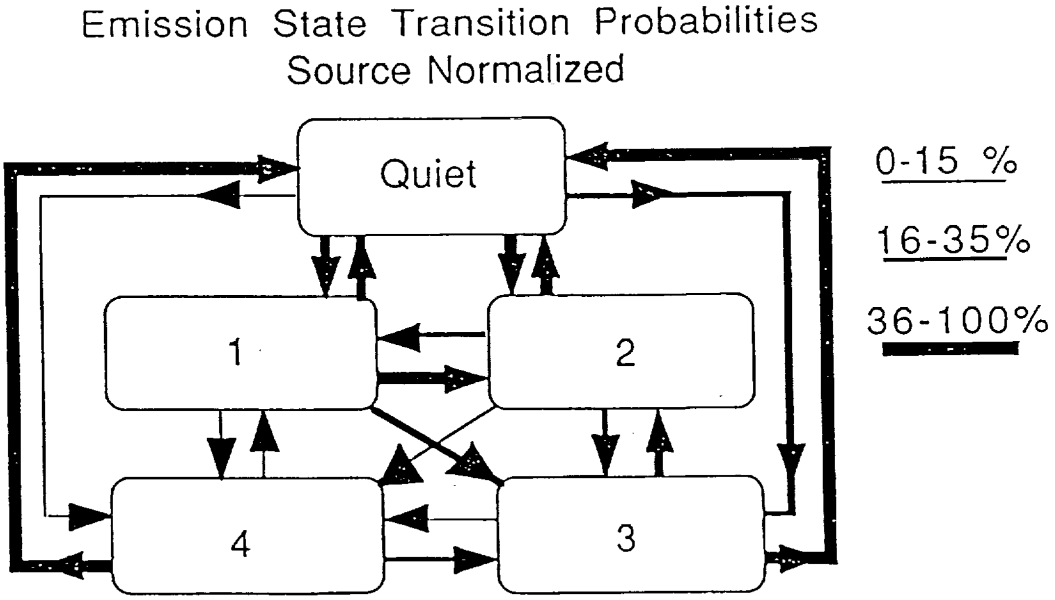

Figure 8. Emission state transition probabilities, source normalized.

Table 3. State Transition Probabilities (Percent) - One Minute Events

		Final State				
		1	2	3	4	5
Initial State	1	89	4.9	2.4	0.6	2.4
	2	5.0	84	3.1	1.2	6.3
	3	0	2.6	86	0.8	11
	4	1.8	0	3.6	85	9.0
	5	0.1	0.2	0.1	~0	99+

The flow charts in Figures 7 and 8 also illustrate the characteristics of the transitions rather well. The null state is most often reached from high frequency cutoffs (36%). In turn, it most often evolves into chaotic striations (43%). The chaotic striations most often return to the null state (40%), or go to high frequency cutoffs (20%) or ordered striations (32%). The ordered striations, in turn, rely chiefly on the null state (38%) and chaotic banding (44%) as evolutionary sources, and return most often to the chaotic state (44%). Type 3 events generally derive with equal probability from all states (20-30%), yet evolve most often into the null state (73%). Events of the fourth type typically derive from chaotic striations (2%) or the null state (38%), and evolve either to high frequency cutoffs (25%) or disappear into nothingness (63%). Again, the implications of these patterns are as yet unclear.

In conclusion, non-thermal Uranian radio emissions can be divided into five major classes according to their spectra, though two of the classes behave similarly and are treated as one in the study of transition probabilities between forms of emission. It is seen that the resulting four types of emission exhibit distinct patterns in their transitions to and from one another and a fifth state defined as a complete lack of planetary signal. The emissions also appear to be linked in longitude to the Uranian south magnetic pole (48 degrees longitude), confirming work by several authors.

IV. Nonthermal Radio Emission from Neptune

Narrowband strongly polarized radio bursts were observable by Voyager 2 from Neptune for more than a 50-day period, ranging from 100 to 1300 kHz. Smoother emission 20-865 kHz was observable for about 10 days near closest approach implying a rotation period of ~16 hours. These additional results were describd by Warwick et al. (1989).

A. Introduction

The Neptunian radio emissions observed by the Planetary Radio Astronomy Experiment (PRA) [Lang and Peltzer, 1977] on the Voyager-2 spacecraft were sufficiently strong to provide unambiguous spectra at 6-sec time resolution only for a few hours immediately before and after closest approach; these spectra are described below. During this period the Neptunian spectra included smooth emission in the frequency range 20-865 kHz (Warwick et al., 1989), which was observed nearly continuously using many 1-kHz wide channels spaced at 19.2 kHz.

More detailed spectral analysis of this emission near encounter reveals that it consists principally of emission bands having widths ranging from a few to several hundred kilohertz. Of great interest is the degree to which the spectral morphology of these banded spectral emissions resembles that of similar emissions observed at Uranus, Saturn, and Jupiter. These three planets all exhibited widely prevalent emissions characterized by multiple narrow bands of emission which tended to drift, or change intensity, on time scales as short as 6 seconds. In the case of Jupiter and Saturn the spectral features can exhibit a systematic asymmetry; the low-frequency wings of these spectral features are often more sharply bounded than are the high-frequency wings, but not the reverse. This asymmetry was not evident in the Neptunian spectra, but these spectral features were often not fully resolved.

One spectral feature of Neptune not evident in the radio emissions from Jupiter, Saturn, or Uranus is a band of intermediate frequencies where the emitted power is weaker, and which corresponds roughly to magnetospheric shells where several planetary satellites are located; because of the brevity of these observations, this coincidence may be fortuitous.

B. Results

By far the most powerful spectra were observed over one planetary rotation beginning five hours before closest approach and continuing until 6 hours after closest approach; no data were available during the first hour immediately after closest approach. Both periods exhibited emission ranging from near 1 kHz to 600-800 kHz, with typical bandwidths of 30-40 channels. There is no evident preference between left- and right-hand circular polarization. The data was reduced in the same fashion as described above for Uranus.

Each emission episode can be divided into three characteristic periods: the beginning period, the middle period, and the end, where the beginnings of both the first and second episodes appear similar, as do the middle and terminating portions. These three periods for each of the first and second emission episodes are presented in Figures 9, 10, and 11, respectively.

Figure 9 shows 4 frames of eight consecutive 6-second spectra characterizing early stages in the evolution of the main two observed Neptunian radio emission episodes. These emissions seemed to be independent of magnetic longitude or latitude, and were present throughout the period of time that Voyager 2 was within 14 R_N of the planet, except during closest approach. Frames a and c come from the first episode, while b and d come from the

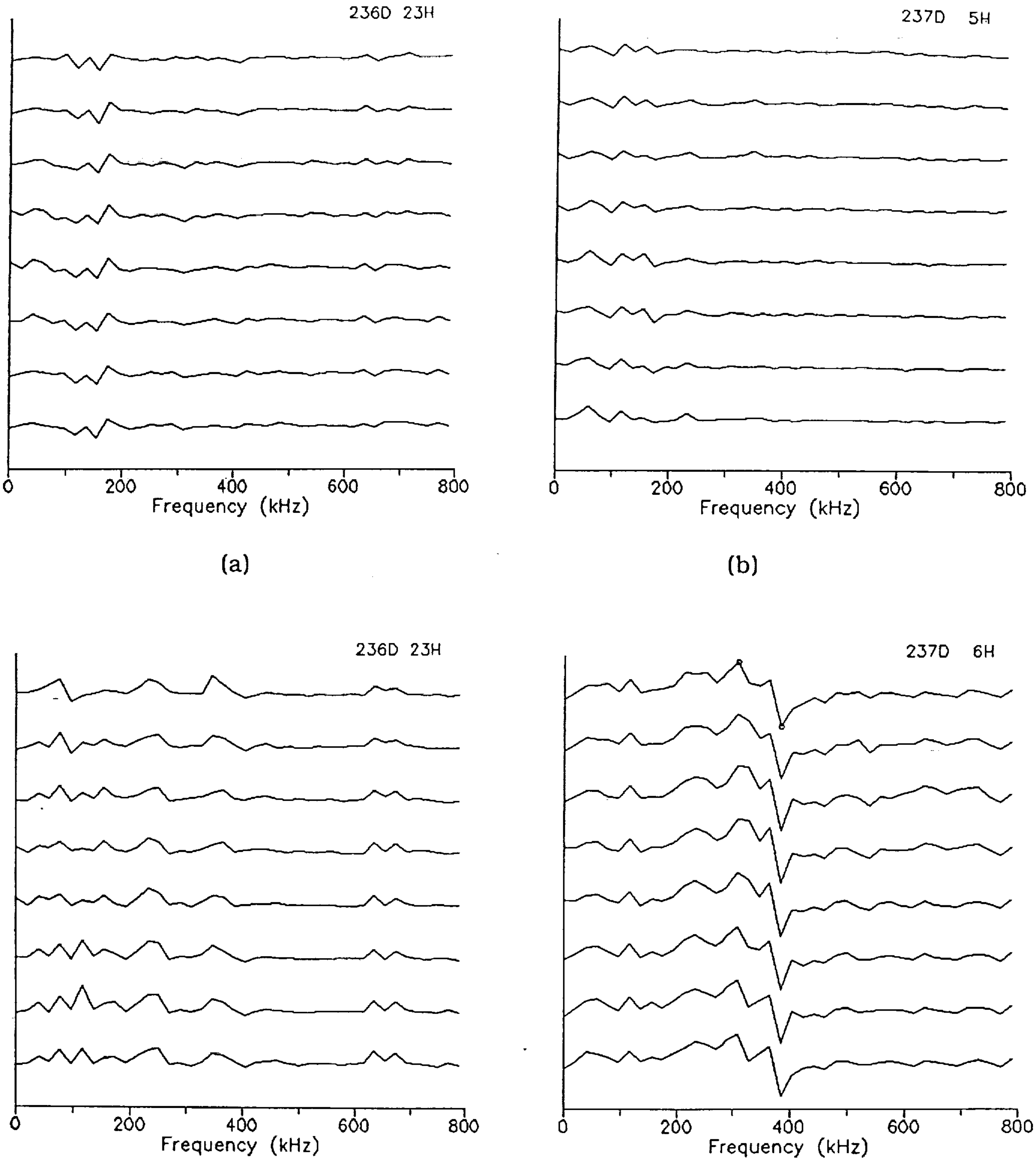

(a)

(b)

(c)

(d)

Figure 9. Early spectra of Neptune emission.

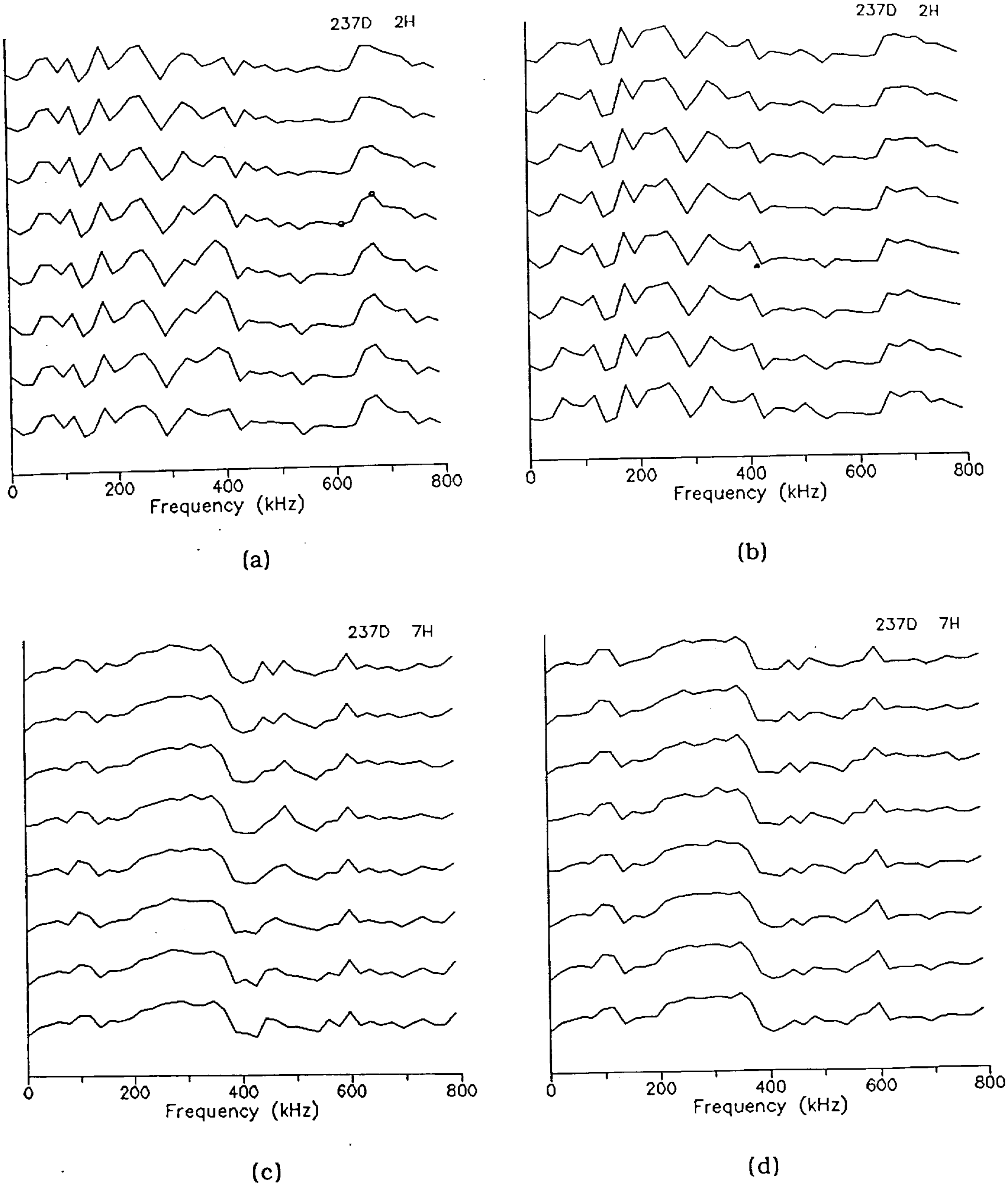

Figure 10. Emission gaps in Neptune spectra.

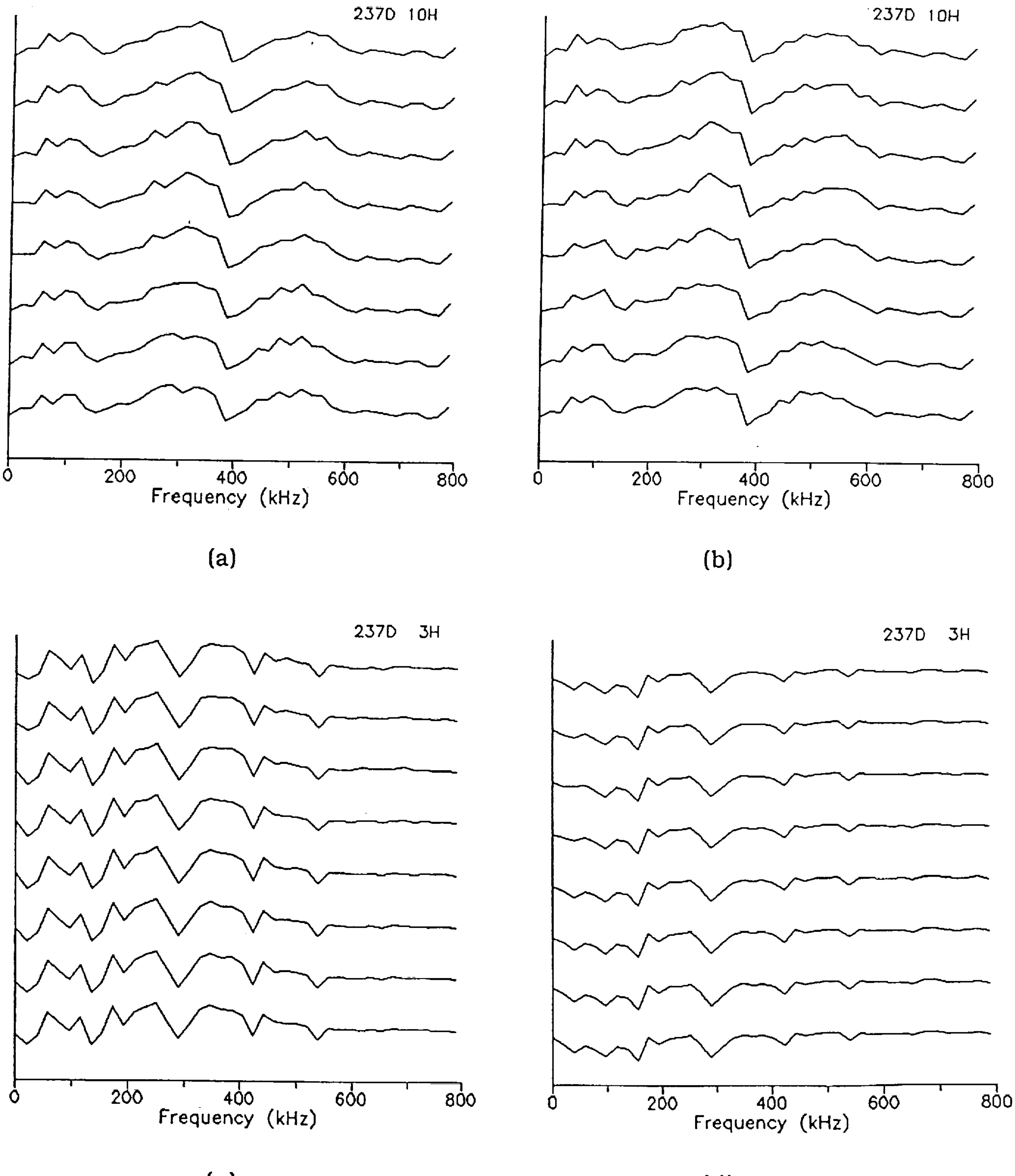

(a) (b)

(c) (d)

Figure 11. Late spectra of Neptune emission.

second. In both a and b, low intensity signals are present below 200 kHz, and more are present between 600 and 800 kHz. These emissions seem to drift in frequency over a time scale of 1 or 2 spectral sweeps (6 sec per sweep). In frame c (32 minutes after a), the signal has increased in power and broadened in frequency, while maintaining the tendency to drift. In frame d (taken about 60 minutes after b), the bandwidth and frequency have also increased from b. Though the signal continues to drift (but more slowly) at frequencies below ~360 kHz, a steady feature (a dropoff edge) has developed at around 380 kHz. This appears to be a dominant feature of Neptunian emissions. In the top (earliest) spectrum of frame d, there are two circles, one at a local maximum of signal, and the other at a local minimum. Although there is some uncertainty regarding definitions, it appears that the power values at these two marked points are 165 millibels (mB) and 52 mB, respectively.

Figure 10 has four frames showing the emission "gap" phenomenon at Neptune. Frames a and b come from the first emission episode, while c and d come from the second. In all four frames, there is a high intensity signal below about 400 kHz and above about 600-700 kHz, with a depression or "gap" in emission intensity in between. In frames a and b, the gap begins at ~420 kHz and ends at ~640 kHz. The high intensity regions show fairly uniform striations that drift only on a time scale of 1/2 or more frames (e.g. 24 seconds +). The gap region shows much weaker signals that also drift, but on a slightly faster time scale (~12 seconds). Note that the two circles in the fourth spectrum of frame are believed to correspond to power levels of 57 mB and 155 mB respectively. In frames c and d, the gap stretches from ~380 kHz to ~600 kHz (the first steady high intensity feature). In the gap, particularly in c, features rise, shift, and fall rapidly (~6 sec) and reach intensity levels near those of the "high intensity" regions. One can also see that some emissions above 800 kHz are cut off by the graph. The peak emission frequency observed was 860 kHz at 237 days, 7 hrs, and 30 minutes. The signal appears above 800 kHz only during the period from 237D 7H to 237D 8H.

Figure 11 has four frames of declining emission taken from the same two Neptunian emission episodes. Frames a and b are from the second episode, while c and d are from the first. Frame a shows very uniform striations with only small emission peaks (around 500 kHz) showing any motion on a time scale of less than 48 seconds (1 frame). Note the similarity to Frame 1d (from the beginning of the same episode). Frame c is very similar to the emissions seen in 2a and 2c (slowly drifting high intensity striations) but without the "gap". Frame 3d, taken ~50 minutes later, shows the same characteristics, but is weaker in intensity. Some time after both frames b and d, both episodes taper off into non-emission.

These figures offer physical models for the emission "gap" seen in Figure 10. Assuming that the depression in emission is due to a decrease in electron population at a certain distance from the planet, thus causing a depression in the intensity of cyclotron emission, we can build such models. Figure 12 is the "tangential emission" model for the gap. Here, it is assumed that the emitting

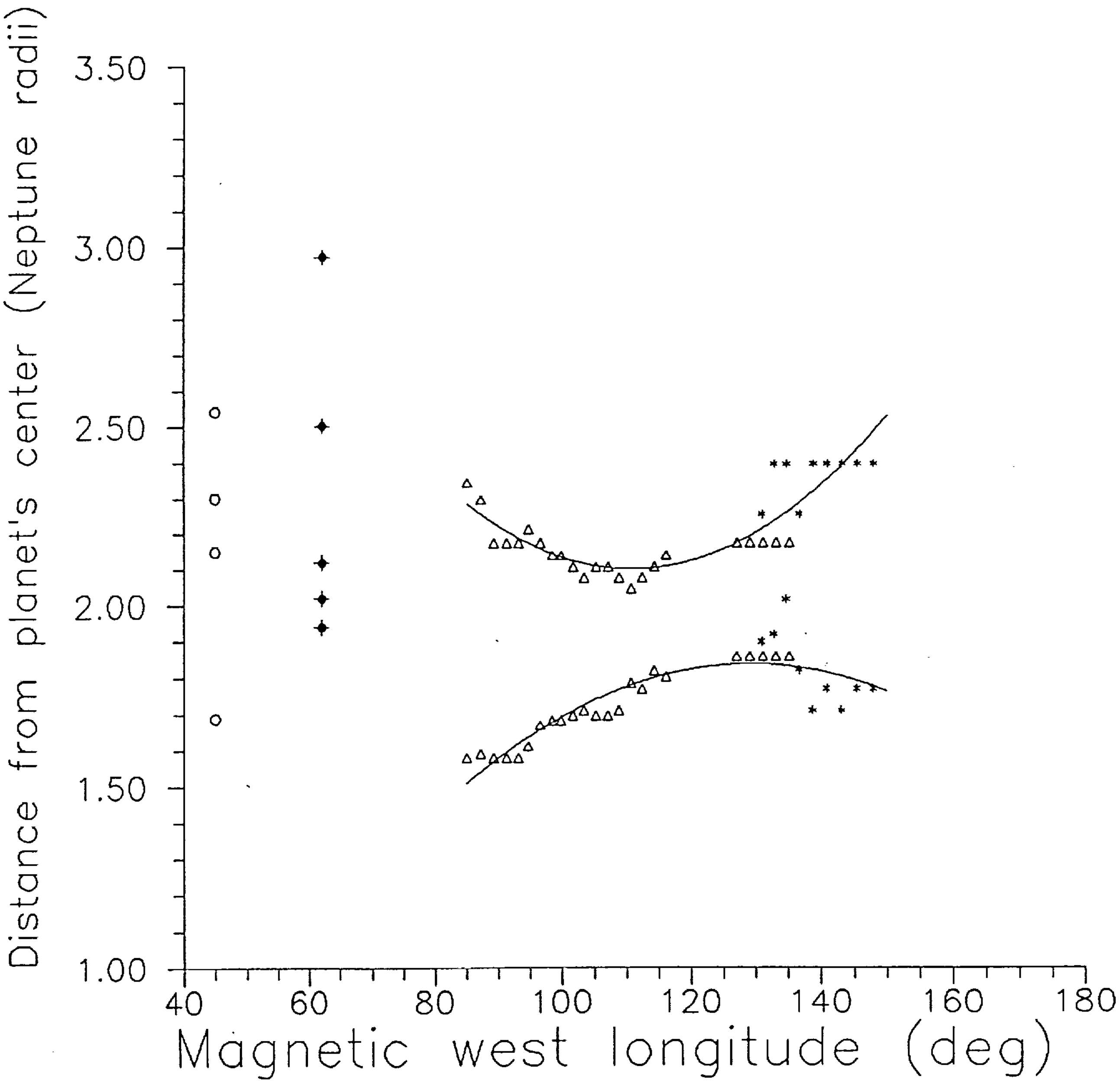

Figure 12. Emission gap boundaries for equatorial tangential emission model.

electrons are located at the magnetic equator. The gap appears to be between 1.5 and 2.00 R_N from the planet's center based on initial magnetic field modes. The triangles denote points from the second emission episode, while asterisks are from the first. The hollow circles denote the orbital radii of Neptune's rings. The filled circles mark the orbital radii of the closest of Neptune's moons. The diameters of these moons are (from closest to farthest) 54 km, 80 km, 180 km, 150 km, and 190 km. Note that while the rings show no significant spatial correlation with the gap, the 3 innermost moons run right through its center. This suggests that the moons may be sweeping electrons from the magnetosphere, thus causing the emission gap. The inner edge of the tangential gap is bounded at 65.4° long., 1.43 R_N and 146.1° long., 1.32 R_N. The outer edge of the tangential gap is bounded at 65.4° long., 12.83 R_N and -176.6° long., 1.70 R_N.

Figure 13 presents the "auroral gap" model, where the emitting electrons are assumed to be at a fixed magnetic latitude somewhere near the magnetic pole. For this model, the latitude was assumed to be 80° (as the angle increases, the gap slowly moves closer in). Here the gap is from about 2.0 to 3.0 R_N. The markings are the same as in Figure 4 (note: both gap edges in both models are fitted with a second-degree polynomial). The inner edge of the auroral gap is bounded at 65.4° long, 1.76 R_N and 146.1° long., 1.63 R_N. The outer edge of the auroral gap is bounded at 65.4° long., 2.26 R_N and -176.6° long., 2.10 R_N.

V. Theoretical Prediction of the Spatial Distribution and Magnitude of the Io-Generated Magnetospheric Currents

A. Introduction

As the Jovian magnetic fields sweep past Io they induce an electric field across it, with the negatively charged surface facing Jupiter. The voltage across Io radially would approach 390 kv in the absence of current flow. This interaction was postulated by Piddington (1967) and others to be a source of energy for the Jovian decametric radio emission and an explanation for the observed dependence of that radiation upon Io's orbital position. More recent analyses by Neubauer (1980) and Herbert (1985) relate the currents generated by Io to this voltage, to the Alfvén conductance of the nearby plasma, and to the conductance of Io and its ionosphere. Here we relate the current distribution to the projected electric surface field strength distribution, and predict the total current I by equating the energy input to its loss through propagation away at the Alfvén velocity.

The spatial distribution of the Io-generated currents can also be estimated by means of simple models combined with energy constraints. The results are

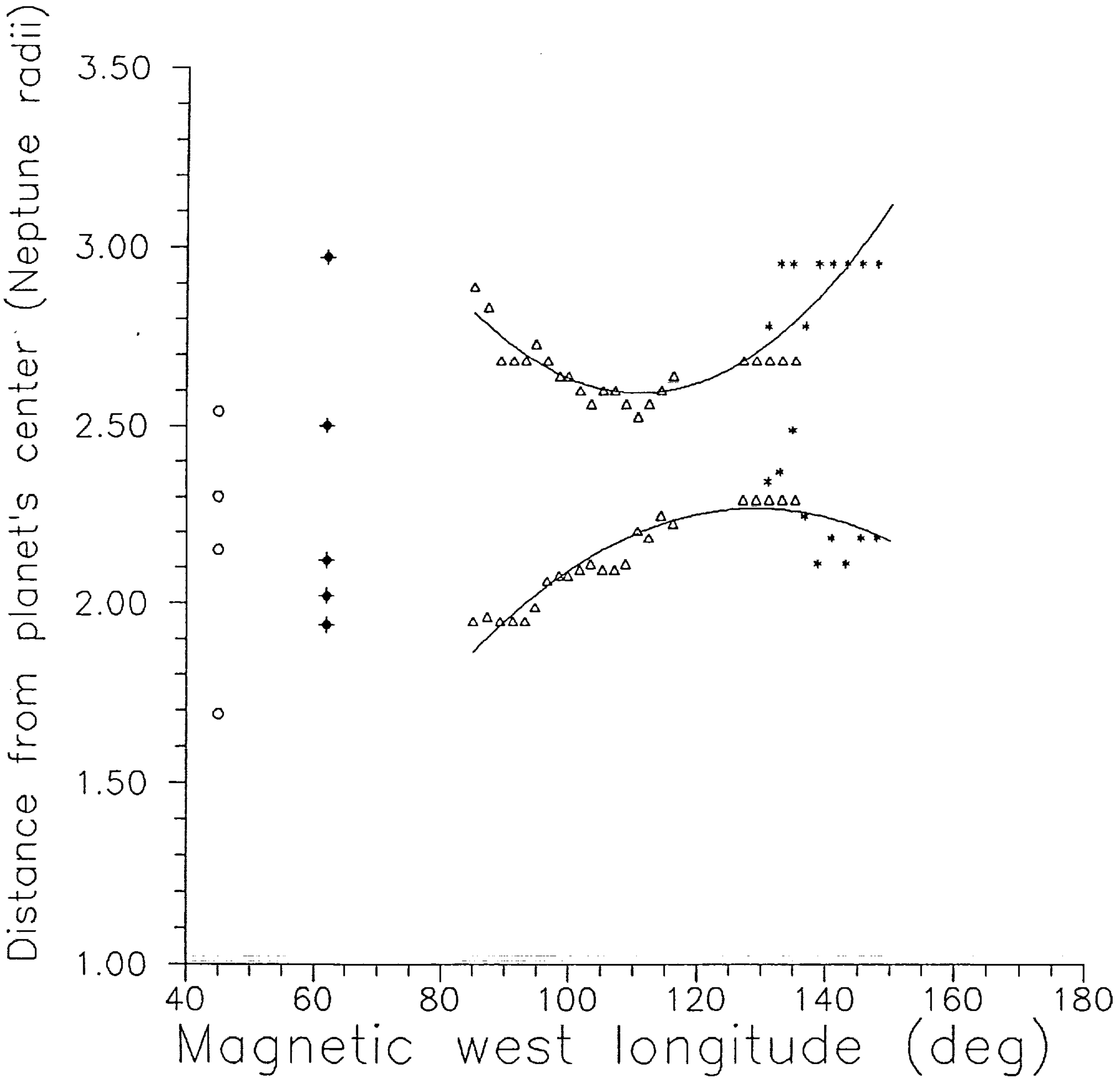

Figure 13. Emission gap boundaries for polar auroral gap emission model.

generally consistent with those cited above, but are more explicit with regard to the spatial distribution of the current. One motive for this prediction of the current distribution is the future study of the microscopic character and behavior of the induced Alfvén waves as they propagate within the Jovian magnetosphere and generate the observed decametric radio radiation.

The approach here is to assume that Io and its ionosphere together comprise an excellent spherical conductor, and that the induced currents flow along the local magnetic field lines in proportion to the local electric fields that inject the charge carriers into the magnetosphere. The power propagated away by the Alfvén wave equals the power supplied by these approximately dipolar electric fields, and thus the total injected current is limited to values consistent with the Alfvén conductance of the ambient plasma.

B. Proposed Model

Under this model the current density **J**(**r**) (a m^{-2}) is controlled near the surface of Io where the conducting electrons are injected into, or attracted from, the Io plasma torus by Io's approximately dipolar electric fields; we assume the total current is limited by inductive effects. The variable **r** is a vector in the x-y plane perpendicular to the local magnetic field. Because the current distribution in Io's frame is reasonably stable, conservation of charge requires that the current along the Alfvén wave near Io be nearly constant and equal to its value at the boundary of Io where most of the charge is injected. We further assume that the radius of the conducting portion of the ionosphere is 1) approximately the same as that of Io, 2) roughly consistent with the scale height observations of Pioneer 10 (Kliore et al., 1974, 1975), which were nominally 60-200 km, and 3) consistent with the plasma density of 5×10^4 cm^{-3} found by Kliore et al. (1975) at the entrance occultation maximum. If we neglect the resistive voltage drop across Io and its ionosphere, then at the surface of Io the electric field strength projected along the unperturbed Jovian magnetic field lines is as shown in Figure 14a. For an assumed background magnetic field of 1.9×10^{-6} T, which is consistent with the data of Acuna et al. (1981), the maximum field strength is approximately 0.16 v m^{-1} projected along the unperturbed magnetic field. As a first approximation we assume that the current density **J**(**r**) is proportional to this field strength.

An additional small electric field will act on charges moving relative to the magnetic field pinned to Io and contributed by the generated current I. Figure 14b presents the total electric field, which has contributions from both the original dipolar electric field and this small inductive term. The inductive term is approximate for it was computed assuming the current was uniform along the z axis, was distributed as shown in Figure 14a, and had magnitude 2.77×10^6 A, which is generally consistent with the observations of Acuna et al. (1981). The net effect of the inductive contribution is to shift the peak of the current distribution slightly to the rear of Io. Figure 14b is also labeled in terms of current density, which is assumed to be proportional to this total electric field

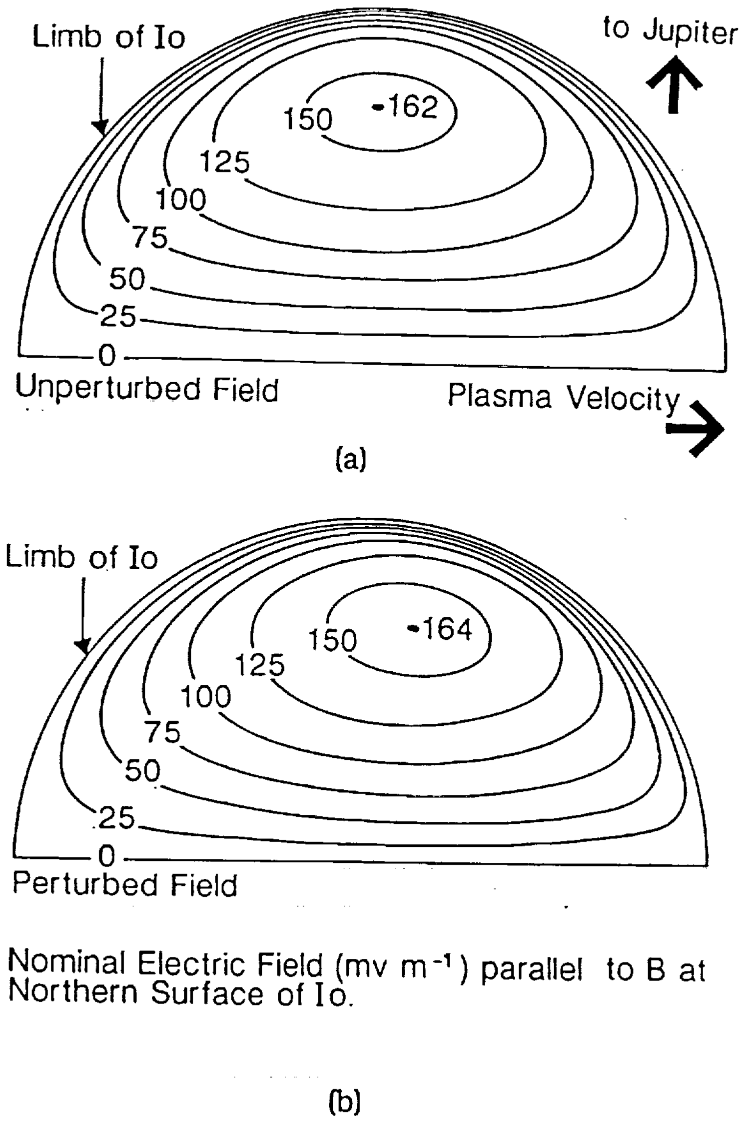

Figure 14. Electric fields near Io: (a) top, unperturbed by currents, (b) bottom, perturbed values.

strength at the surface of Io. Further iterations to refine this electric field strength are unnecessary.

We further assume that **J(r)** is limited by inductive effects such that the delivered power P (the volume integral of the vector dot product of the electric field vector **E** and the current density **J**) equals the power in the escaping Alfvén wave. This wave power P_A is approximately equal to the product of the Alfvén velocity V_A and the total magnetic energy in a one-meter thick slab in the x-y plane. We assume V_A is approximately 253 km s^{-1}, which is the *in situ* value measured by Barnett (1986) near the moment of closest approach for Voyager 1. Since P is proportional to the total induced current I, and P_A is proportional to I^2, equating them yields the current I flowing in each Alfvén wave near Io; this predicted current I is 4.5 x 10^6 A if Io is perfectly conducting. The energy of a travelling Alfvén wave is divided equally between magnetic and kinetic energy. However, most of the energy near Io is magnetic in the wave generation region where $\mathbf{E} \cdot \mathbf{J}$ is large. There is thus a transition region beyond ~1500 km from Io where the magnetic energy diminishes so as to supply and balance the increasing lateral kinetic energy of the magnetospheric ions participating in the wave. Therefore, near the Voyager-1 flux tube encounter point, about 20,000 km south of Io, the magnetic energy density should have diminished by a factor of 2, and the current by a factor of ~2, i.e., to 3.2 x 10^6 A.

This predicted current distribution can be tested by comparing its magnetic fields to those inferred from the Voyager-1 magnetometer measurements. A total current of 2.77 x 10^6 A best matches the magnetic field strengths observed by Acuna et al. (1981). This comparison of the predicted and observed magnetic fields utilized the current distribution of Figure 14b, scaled, and assumed that the lag angle Θ_A of the Alfvén wave was consistent with a nominal Alfvén velocity of 284 km s^{-1}.

Since Io generates waves moving both north and south, the total current through Io is twice I. To reduce this predicted current of 3.2 x 10^6 A to the value of 2.8 x 10^6 A inferred from Voyager 1, the electric field strengths could be reduced proportionately, by a factor of perhaps 0.87. A total resistance across Io and its ionosphere of ~0.01 ohms would accomplish this. Although such a resistance might slightly redistribute the current over Io, it is unlikely the redistribution would be marked. It is interesting to note that even if there were no ionosphere, photoproduction of electrons at Io's surface would be more than sufficient to supply the necessary current densities if the sun were shining. Sunlight reflected from Jupiter might also suffice given its moderate albedo and large subtended solid angle.

This analysis is preliminary, but does suggest the general form of the current distribution generated by Io, which is less shell-like in character than some predictions.

Recent observations of brighter H_3^+ emission excited near the southern foot of the Io flux tube than near the northern foot suggest that the Pederson conductivity of the Jovian ionosphere (greater in the south) may be limiting the Northern current (Connerney et al., 1993). However, the H_3^+ emission may occur at altitudes below those where the current ceases as the Alfvén wave is reflected, i.e. H_3 emission may not be proportional to the power in the associated reflected Alfvén wave which would more likely be reflected by macroscopic currents generated in the ionosphere by Alfvén wave fields rather than by longitudinally moving precipitating electrons. More importantly, causality suggests that ionospheric conductivity is not an issue since Io has long passed before any Alfvén current returns.

References

Acuna, M. H., F. M. Neubauer, and N. F. Ness, Standing Alfvén wave current system at Io: Voyager I Observations, *J. Geophys. Res. 86*, p. 8513, 1981.

Arias, T. A., Modulated spectral activity in the inner Jovian magnetosphere, S.B. thesis, Dept. of Physics, MIT, June 1986.

Barnett, 1986.

Connerney, J. E. P., R. Baron, T. Satch, and T. Owen, Images of excited H_3^+ at the foot of the Io flux tube in Jupiter's atmosphere, *Science 262*, 1035-1038, 1993.

Curtis, S. A., M. D. Desch, and M. L. Kaiser, The radiation belt origin of Uranus' nightside radio emission, *J. Geophys. Res. 92*, pp. 15199-151205, 1987.

Desch, M. D., and M. L. Kaiser, Ordinary mode radio emission from Uranus, *J. Geophys, Res. 92*, pp. 15211-15216, 1987.

Eikenberry, S. S., Spectral phenomenology of Neptunian radio emissions, S.B. thesis, Dept. of Physics, MIT, June 1990.

Evans, D. R., J. H. Romig, and J. W. Warwick, Bursty radio emissions from Uranus, *J. Geophys. Res. 92*, pp. 15206-15210, 1987.

Garnavich, P. M., Jovian decametric radiation: A test of the multiple-reflection Alfvén wave model, S.M. thesis, Dept. of Physics, MIT, June 1983.

Goldstein, M. L., A. Eviatar, and J. R. Thieman, A beaming model of the Io-independent Jovian decameter radiation based on multipole models of the Jovian magnetic field, *Astrophys. J. 229*, pp. 1186-1197, 1979.

Goldstein, M. L., and J. R. Thieman, On the formation of arcs in the dynamic spectra of Jovian decameter bursts, *J. Geophys. Res. 86*, pp. 8569-8578, 1981.

Gulkis, S., and T. D. Carr, The main source of radio emission from the magnetosphere of Uranus, *J. Geophys, Res. 92*, pp. 15159-15168, 1987.

Gurnett, D. A., and C. K. Goertz, Multiple Alfvén wave reflections excited by Io: Origin of the Jovian decametric arcs, *J. Geophys. Res. 86*, pp. 717-722, 1981.

Hashimoto, K., and M. L. Goldstein, A theory of the Io phase asymmetry of the Jovian decametric radiation, *J. Geophys. Res. 88*, pp. 2010-2020, 1983.

Herbert, 1985.

Kaiser, M. L., M. D. Desch, and S. A. Curtis, The source of Uranus' dominant nightside radio emissions, *J. Geophys. Res. 92*, pp. 15169-15176, 1987.

Kliore, *et al.*, Preliminary results on the atmospheres of Io and Jupiter from the Pioneer 10 S-band occultation experiment, *Science 183*, p. 323, 1974.

Kliore, *et al.*, 1975.

Lang, G. J., and R. G. Peltzer, Planetary radio astronomy receiver, *IEEE Trans. Aerosp. Electron. Syst. AES13*, pp. 466-472, 1977.

Leblanc, Y., On the arc structure of the DAM Jupiter emission 1981, *J. Geophys. Res. 86*, pp. 8546-8560, 1981.

Leblanc, Y., and F. Genova, The Jovian S burst sources, *J. Geophys. Res. 86*, pp. 8564-8568, 1981.

Lecacheux, A., and A. Oretega-Molina, Polarization and localization of the Uranian radio sources, *J. Geophys. Res. 92*, pp. 15148-15158, 1987.

Ness, N. F., M. H. Acuna, K. W. Behannon, L. F. Burlaga, J. E. P. Connerney, R. P. Lepping, and F. M. Neubauer, Magnetic fields at Uranus, *Science 233*, pp. 85-89, 1986.

Neubauer, F. M., Nonlinear standing Alfvén wave current system at Io: Theory *J. Geophys. Res. 85* , 1171-117, 1980.

Piddington, J. H., Jupiter's magnetosphere, *Rep. 67-63*, Univ. of Iowa, Iowa City, 1967.

Staelin, D. H., Character of the Jovian decametric arcs, *J. Geophys. Res. 86*, pp. 8581-8584, 1981.

Staelin, D. H., P. M. Garnavich, and Y. Leblanc, Jovian decametric arcs and

Alfvén currents, *J. Geophys. Res. 93*, pp. 3942-3948, 1988.

Stone, E. C., and E. D. Miner, The Voyager 2 encounter with the Uranian system, *Science 233*, pp. 39-43, 1986.

Thieman, J. R., J. K. Alexander, T. A. Arias, and D. H. Staelin, Striated spectral activity in Jovian and Saturnian radio emission, *J. Geophys. Res. 93*, A9, pp. 9597-9605, 1988.

Warwick, J. W., *et al.*, Voyager 2 radio observations of Uranus, *Science 233*, 102-106, 1986.

Warwick, J. W., *et al.*, Voyager Planetary Radio Astronomy at Neptune, *Science 246*, pp. 1498-1502, 1989.

Zarka, P., and A. Lecacheux, Beaming of Uranian nightside kilometric radio emission and inferred source location, *J. Geophys. Res. 92*, pp. 15177-15187, 1987.